Optimal Design of a Transformer-based Solid-State Pulse Modulator with a Damping Network for Ultra-Fast Rise Times

Conference Paper

Author(s):
Stathis, Spyridon; Biela, Jürgen (iD)

Optimal Design of a Transformer-based Solid-State Pulse Modulator with a Damping Network for Ultra-Fast Rise Times

Spyridon Stathis and Juergen Biela
Laboratory for High Power Electronic Systems, ETH Zürich
stathis@hpe.ee.ethz.ch

Keywords

"Pulse Transformer", "Solid-State Pulse Modulator", "Damping Network", "Optimization"

Abstract

This paper presents an optimization procedure for a transformer-based solid-state pulse modulator with an additional damping network at the load. The design of the pulse transformer and the damping network are combined in the procedure, so that pulses with pulse lengths in the µs-range with a fast rise time and a compact transformer volume can be achieved.

1 Introduction

Solid-state pulse modulator systems are key elements in many particle accelerator facilities. There, the modulator system must be able to generate precise voltage/current pulses with fast rise and fall times, and a low ripple as well as overshoot. A possible modulator concept, which meets these requirements, are solid-state pulse modulators based on pulse transformers. These have been proven to be able to produce high voltage pulses at high power levels [1–5] and achieve a high efficiency [6].

In transformer-based modulators, the achievable parameters of the pulse strongly depend on the parasitic components of the transformer and the load, and these parasitics could lead to undesired resonances [7]. Moreover, the unwanted parasitics might result in a pulse which does not meet the required specifications, that is for example, the rise time is too high. For mitigating this problem, various damping network concepts have been proposed for different pulse lengths and rise times, which offer effective damping of the pulse and force it to lie inside the demanded specifications. For example, in [8, 9] pulses with a rise time of tens of µs and with a length of a few µs are investigated and the presented damping network is based on passive circuit elements only. In [10, 11], a hybrid damping network is presented for applications, which require pulses in the ms/s range and with a rise time of hundreds of µs. The hybrid damping network consists of active switches and passive components.

However, damping networks have not been examined for pulse transformer-based modulator topologies and for short pulse lengths with rise times in the range of 1 µs. Furthermore, the design of the damping circuits has not been included into a general system optimization as given in [5], which enables to identify the best set of design and operating parameters of the modulator system. Therefore, the goal of this paper is to propose an extension of the optimization procedure presented in [5], which combines the design of the transformer and the design
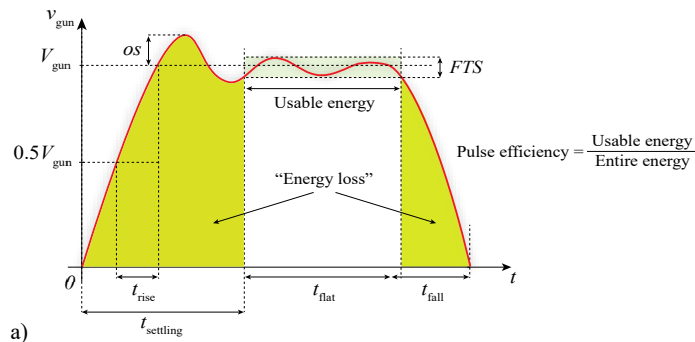

Table I: CARM modulator specifications

Symbol	Parameter	Value	
V_{gun}	Pulsed voltage	700 kV	Electrical pulse parameters
I_{gun}	Pulsed current	8 A	
P_{gun}	Pulsed power	5.6 MW	
t_{flat}	Pulse length	5 µs	Pulse shape parameters
t_{rise}	Rise time (50%-100%)	≤1 µs	
$t_{settling}$	Settling time	≤5 µs	
os	Overshoot	0%	
FTS	Flat-top stability	≤0.1%	
ΔV	Ripple	≤0.1%	
f_{rep}	Repetition frequency	10 Hz	
C_{gun}	Gun capacitance	100 pF	Gun parameters
R_{gun}	Gun resistance	87.5 kΩ	

Fig. 1: a) Voltage pulse shape including the definition of the main parameters. During t_{settle} and t_{fall} "energy losses" occur as this energy can not be used for the application. Once the voltage pulse lies within FTS, the flat-top interval t_{flat} begins. The ratio of the usable energy to the entire pulse energy defines the pulse efficiency. Table I lists the specifications of the considered CARM modulator [12].
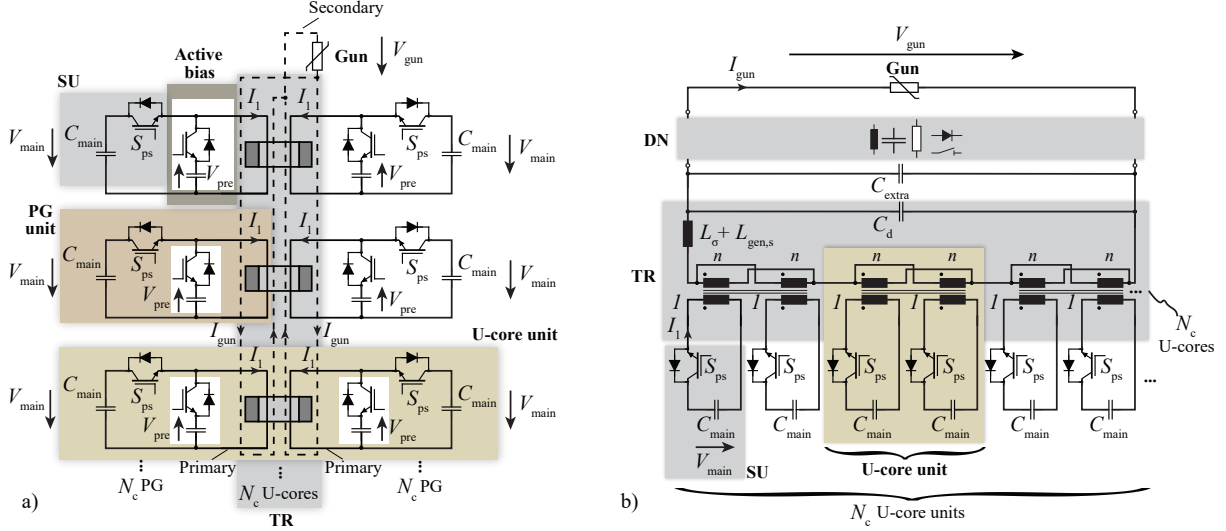
Fig. 2: a) Basic pulse transformer-based solid-state modulator consisting of U-core units, two parallel connected secondary windings and the gun. b) Electrical equivalent circuit of the solid-state modulator including the transformer with its parasitics, the leakage inductance L_σ and the capacitance C_d, the switching units inductance $L_{gen,s}$ referred to the secondary side, the considered extra capacitance C_{extra}, the possible damping network and the gun. The active bias circuits are omitted for simplification.

of the damping network for a transformer-based solid-state modulator. The proposed optimization enables to comprehensively compare different damping network topologies and their influence on the transient characteristics of the pulse, its efficiency as well as the transformer volume. By using this approach, the designer can decide whether the insertion of a damping circuit is beneficial for the performance of the system as well as which damping network leads to the best pulse efficiency and minimum transformer volume at the same time. To validate the performance of the general design methodology, the CARM source modulator is used as a case study [12] and a feasibility study for the design of the system is performed. A set of challenging specifications need to be fulfilled for this application, which are listed in Table I. In Fig. 1a), an indicative scheme of the voltage pulse is provided, where the general specifications of the pulse are defined.

The structure of the paper is as follows: In section 2, the basic pulse transformer-based modulator topology including the damping network is briefly explained. Section 3 describes the extension of the optimization procedure which is used for designing the modulator with damping network. In section 4, results and considerations are given for the CARM modulator system. Finally, section 5 summarizes the main outcomes of the presented work.

2 Basic Pulse Transformer-based Solid-State Modulator Topology

The considered pulse transformer-based topology is shown in Fig. 2a). It is based on the split-core pulse transformer concept, which is also often called as matrix transformer [7, 13]. The switching units (SU) consist of the main capacitors C_{main}, which are charged up to V_{main}, and the pulse switches S_{ps} (here IGBTs are assumed). For premagnetizing the cores of the pulse transformer (TR) and reducing the core volume, often active bias circuits are used [14]. To double the pulsed power rating and reduce the leakage inductance, two pulse generators (PG) units can be mounted on the two legs of the considered U-cores. The core with the two primary windings and the two SUs results in a so called U-core unit. The two parallel connected secondary windings enclose the core legs of all the N_c U-cores, where N_c denotes the number of U-cores. For a matrix transformer, the required number of turns N_2 of the secondary winding is given as

$$N_2 = \frac{V_{gun}}{V_{main}} \cdot \frac{N_1}{N_c} \xrightarrow{n = \frac{V_{gun}}{V_{main}}} \frac{N_2}{N_1} = \frac{n}{N_c} \tag{1}$$

where n is the ratio between the gun voltage and the main capacitor bank voltage (voltage ratio) and N_1 is the number of turns of the primary winding.

In Fig. 2b), the electrical equivalent circuit of the topology in Fig. 2a) is given, which also includes a possible damping network (DN). The active bias circuits are excluded in the following analysis as they do not, significantly, influence the pulse performance in case a bipolar magnetic flux swing in the core is assumed, which leads to a transformer with reduced core cross-sectional area [14]. In the equivalent circuit, the leakage inductance L_σ and the distributed capacitance C_d of the transformer are referred to the secondary side. The parasitic inductance of the
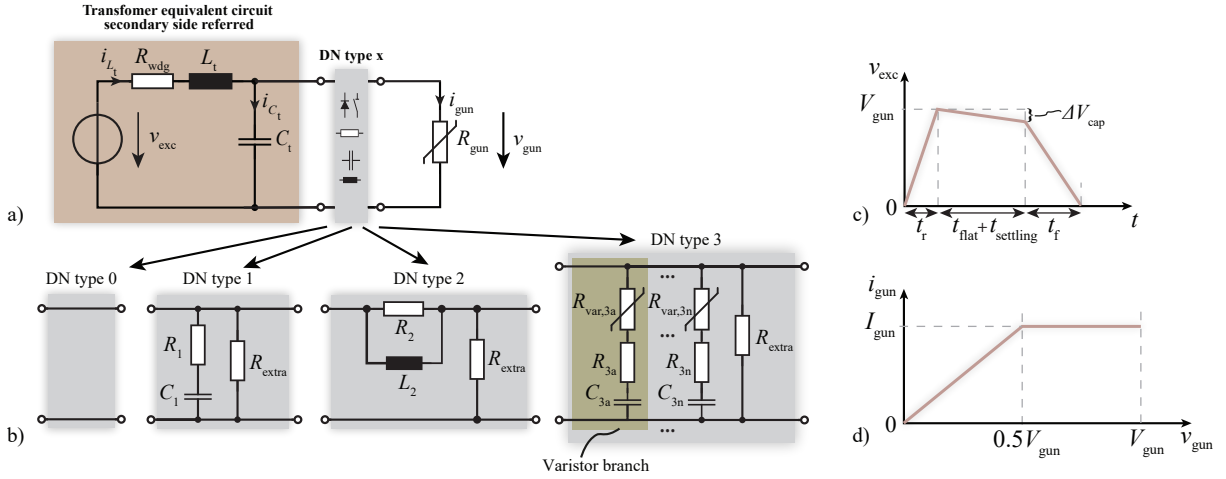
Fig. 3: a) Simplified secondary side referred equivalent circuit of the solid-state pulse modulator with a damping network. The resistance of the windings is included as R_{wdg}. b) Possible damping network configurations. Type 0 denotes the case if no damping network is used. c) Applied voltage referred to the secondary side, which models the transient and the steady state behaviour of the switching unit. d) Current-voltage characteristic of the gun.

SUs L_{gen} is also included in the equivalent circuit as it adds a significant amount of inductance. Given the parallel connection of the SUs on each core, L_{gen} is halved. Transferring L_{gen} to the secondary side of the transformer results in

$$L_{gen,s} = N_c \frac{L_{gen}}{2} \left(\frac{N_2}{N_1}\right)^2 \overset{(1)}{=} \frac{L_{gen}}{2} \cdot \frac{n^2}{N_c} \tag{2}$$

Capacitance C_{extra} models the parasitic capacitance which appears on the secondary side of the transformer in addition to C_d. This includes the capacitance of the gun C_{gun} and the capacitance of the capacitive voltage divider $C_{divider}$ which is used for measuring the pulse voltage. In case a high voltage cable connects the transformer to the gun, the capacitance of the cable must also be added to C_{extra} as described in [5]. The damping network (DN) is connected to the secondary side between the load and the transformer and it may consist of passive elements only or a combination of switches/varistors and passive elements (hybrid).

In order to evaluate the performance of the voltage pulse, the modulator circuit in Fig. 2b) is modelled by the simplified secondary side referred equivalent circuit of Fig. 3a). The total parasitic inductances and capacitances are included in the quantities L_t and C_t as

$$L_t = L_{gen,s} + L_\sigma \qquad C_t = C_d + C_{extra} \tag{3}$$

The magnetizing inductance and the iron losses are assumed to have negligible influence due to the fast rise time [7]. The circuit is excited by a voltage source v_{exc}, as shown in Fig. 3c), which is a linear approximation of the switching and the steady state behaviour of the IGBT having a rise time t_r and a fall time t_f. An additional slope ΔV_{cap} during the time interval $t_{flat} + t_{settling}$ is inserted, which models the voltage droop of the main capacitors. The droop is approximately given as

$$\Delta V_{cap}\% = \frac{(t_{flat} + t_{settling})I_{gun}}{C_{main,s}} \cdot \frac{1}{V_{gun}} 100\% \tag{4}$$

where $C_{main,s}$ is the value of the total main capacitance C_{main} of all PG units transferred to the secondary side as

$$C_{main,s} = 2C_{main} \frac{N_c}{n^2} \tag{5}$$

The voltage droop results in a more limited flat-top stability FTS_{lim}, which is given as $FTS_{lim} = FTS - \Delta V_{cap}\%$, with FTS being defined in the specifications of the application. The value of C_{main} must be chosen, so that $\Delta V_{cap}\% \ll FTS$ in order to limit the impact of the droop on the pulse shape. A possible droop compensation is not considered in this paper in order to simpilfy the analysis.

The considered damping network types are shown in Fig. 3b). DN type 0 denotes the case when no damping network is present while DN type 1 and 2 consist of passive elements only. The DN type 3 is an expansion of DN type 1 having non-linear elements, such as varistors, in series with RC components. The $R_{var,3a}$-R_{3a}-C_{3a} elements
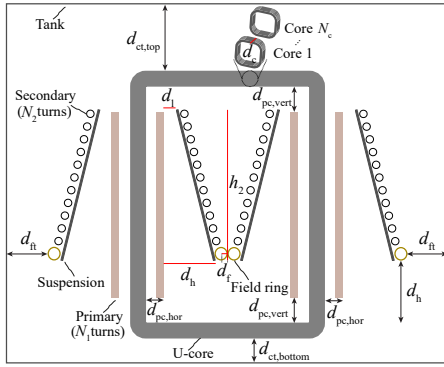
Table II: Considered degrees of freedom and parameters for the CARM transformer optimization

Symbol	Parameter	Value/Expression	
d_h	HV side distance	$120\,\text{mm} \leq d_h \leq 160\,\text{mm}$	
d_l	LV side distance	$10\,\text{mm} \leq d_l \leq 40\,\text{mm}$	
d_c	Core depth	$140\,\text{mm} \leq d_c \leq 200\,\text{mm}$	5 degrees of freedom
$h_{2,\text{add}}$	Additional secondary winding height	$10\,\text{mm} \leq h_{2,\text{add}} \leq 100\,\text{mm}$	
N_c	Number of cores	1-3	
d_f	Field ring radius	9 mm	
B_{ap}	Applied flux density	1.5 T	
$d_{\text{pc,hor}}$	Horizontal distance core & primary winding	4.5 mm	
$d_{\text{pc,vert}}$	Vertical distance core & primary winding	15 mm	
$d_{\text{ct,bottom}}$	Bottom distance core & tank	15 mm	
$d_{\text{ct,top}}$	Top distance core & tank	50 mm	Considered parameters
d_{ft}	Distance field ring & tank	$d_h + 40\,\text{mm}$	
N_1	Primary winding turns	1	
$\varepsilon_{\text{r,oil}}$	Mineral oil relative permittivitty	3.2	
E_{th}	E-field threshold	$20\,\text{kV}\,\text{mm}^{-1}$	
t_r/t_f	IGBT rise/fall time	200 ns	
C_{divider}	HV divider capacitance	50 pF	

Fig. 4: a) General 2-D representation of the transformer geometry where the optimization and geometrical variables are defined. A tilted winding arrangement is used for a reduced leakage inductance [7]. Table II lists the optimization variables, the predefined geometrical and considered parameters for the CARM modulator.

form a varistor branch. Many varistor branches can be connected in parallel to the gun. The gun has a current-voltage characteristic as illustrated in Fig. 3d). Up to half of the nominal pulse voltage, the gun current shows a resistive behaviour. When $v_{\text{gun}} > 0.5 V_{\text{gun}}$ the gun current is equal to the rated current I_{gun} which remains constant, limited by the emitter temperature.

3   System Optimization Procedure

The extended system optimization procedure is outlined in Fig. 5. The optimization procedure is based on the routine presented in [5], which is extended by the additional damping network design step for optimizing the DN topology and parameters. In the following, the workflow of the routine is given. For better understanding the routine, Fig. 4a) is provided, showing a 2-D representation of the transformer geometry as well as the Table II, which contains the considered degrees of freedom and predefined parameters.

3.1   Transformer Design

At the beginning of the routine (S1), the ranges of the degrees of freedom, the pulse specifications as well as some predefined geometrical parameters are defined (Table II). Five degrees of freedom are selected which are the distance between primary and secondary winding at the HV and LV side, d_h and d_l respectively, the depth of the core d_c, the additional height of the secondary winding $h_{2,\text{add}}$ and the number of cores N_c. In S2, the number of turns of the primary winding N_1 is selected resulting in a minimum secondary winding height. This is added to $h_{2,\text{add}}$ to get the total height of the secondary winding h_2. Next, the cross-sectional area of a single core, using the volts-seconds of the pulse voltage, the effective magnetic path length and other quantities (e.g core dimensions) are calculated, which result in the tank and the transformer volume. The procedure continues with the calculation of the maximum E-field E_{max} on the surface of the conductors with the highest potential (S3) and then it is checked, whether E_{max} is smaller than the permissible E-field E_{th}. The charge simulation method is used for the maximum E-field calculation [15]. In case E_{max} is higher than E_{th}, a new set of degrees of freedom is chosen. If $E_{\text{max}} < E_{\text{th}}$, the calculation of the winding losses
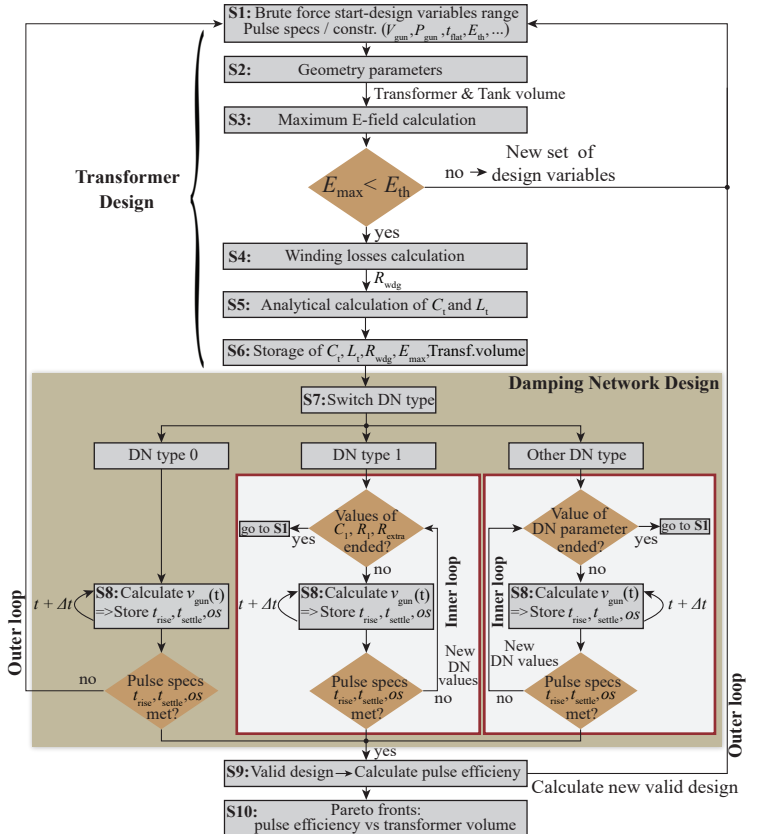

Fig. 5: Proposed optimization procedure flowchart including the damping network design section.

and the extraction of the total secondary-referred winding resistance R_{wdg} follows in S4. The winding losses due to the skin and the proximity effect have been studied extensively in [16] for foil and round conductors. Here, it is assumed that both windings cover the entire core window height. In order to simplify the model for the pulse current, a trapezoidal shape is assumed with a rise time of 1 µs and a flat-top of 5 µs. This current is analyzed with a Fourier series with 100 harmonics in order to calculate the skin depth. The secondary round turns are transformed to a foil conductor for calculating the proximity effect losses as described in [16]. Finally, the AC resistance of all the windings is computed at the fundamental frequency f_{rep}.

In a next step, the extraction of the transformer parasitics follows in S5. The primary foil winding is approximated by N_2 parallel connected round conductors equally distributed over the primary winding height for minimizing the distance between adjacent conductors [17]. Moreover, a homogeneous current distribution is considered and the primary and secondary windings are grounded at the LV side. The leakage inductance L_σ is then calculated with the current mirroring method [18] and is added to the generator inductance $L_{\mathrm{gen,s}}$, which results in the total parasitic inductance L_t. For the distributed capacitance C_d of the transformer, the charge simulation method is used [15], which takes into account the grounded surfaces of the core and tank. A detailed explanation of the steps for calculating C_d can be found in [17]. The capacitance of the gun and the capacitance of the HV divider are added to C_d in order to obtain the total parasitic capacitance C_t which appears on the secondary side of the transformer.

In step S6, the total parasitic inductance and capacitance, the resistance of the windings, the maximum E-field and the transformer volume are stored for each considered core number N_c. With the stored values, the Pareto fronts of the transformer parasitics are obtained. The ranges of the transformer parasitics L_t and C_t obtained from the Pareto fronts are used afterwards to solve the circuit in Fig. 3a) analytically for each DN type independently of the transformer design. This methodology is used as the number of iterations rapidly increases if the design of the DN types is directly included inside the optimization cycle of the transformer design. For instance, the design of the transformer and the design of the DN type 1 would require $L = D + P = 8$ nested loops, where $D = 5$ stands for the number of loops due to the 5 transformer degrees of freedom and $P = 3$ is the number of loops because of the three different parameters of the DN type 1, i.e the R_1, C_1 and R_{extra} values. Knowing the lower and upper boundaries of the parasitics for each transformer core number results in a lower total number of iterations. Therefore, a more extensive parametric sweep can be performed for the parameters of the damping network.

3.2   Damping Network Modeling & Design

In the next step, the damping network is designed. First, the DN type is selected in step S7 and depending on the selection, the output voltage pulse $v_{\mathrm{gun}}(t)$ is calculated in step S8. To describe the detailed steps inside the DN section, the DN type 1 is used as an example. Neglecting the influence of the core and the winding resistance and assuming a resistive load at the output, the transformer is essentially an undamped 2nd order LC network. In [19], the following set of equations is used to damp the oscillations of an LC input stage with a shunt RC branch (i.e DN type 1), which is inserted in front of a converter system. With the characteristic resistance R_0, and the ratio of the capacitors α

$$R_0 = \sqrt{\frac{L_t}{C_t}} \qquad \alpha = \sqrt{\frac{C_1}{C_t}} \tag{6}$$

the optimum resistance ratio $Q_{\mathrm{opt,\ type\ 1}}$ and the optimum damping resistance R_1 are given as [19]:

$$Q_{\mathrm{opt,\ type\ 1}} = \frac{R_1}{R_0} = \sqrt{\frac{(2+\alpha)(4+3\alpha)}{(4+\alpha)2\alpha^2}} \Rightarrow R_1 = R_0 \sqrt{\frac{(2+\alpha)(4+3\alpha)}{(4+\alpha)2\alpha^2}} \tag{7}$$

However, this design methodology is not completely suitable for the design of the DN type 1 for the CARM modulator due to the nonlinear current-voltage characteristic of the gun and the fact that there is not an ideal controller which regulates the voltage pulse. Hence, this methodology is only used as a first indication for the right range of the R_1 and C_1 values. In order to evaluate how the DN type 1 affects the voltage pulse, R_1, C_1 and R_{extra} are varied over different values.

By inserting the variable resistor R_{extra}, the high impedance of the gun is decreased in order to improve the shape of the voltage pulse at the cost of higher power losses. This may lead to more SUs in parallel at the primary side and to a multi-core arrangement for the pulse transformer. Consequently, the role of R_{extra} in the pulse damping and whether it is beneficial for the system performance is examined in the following.

3.3   Pulse Shape Analysis

In the optimization cycle, the circuit of Fig. 3a) with the DN type 1 is analyzed in the time domain solving the differential equations numerically. Because of the time domain analysis of the circuit, the model can be used

with any given linear or non-linear load. The circuit analysis of Fig. 3a) leads to the following set of differential equations with the state vector $\bar{x}_{\text{type 1}}$ containing the states of the system, i.e the currents through the inductors and the voltages of the capacitors. Hence,

$$\bar{x}_{\text{type 1}} = \left[i_{L_t},\ v_{C_t},\ v_{C_1} \right]^{\mathrm{T}} \tag{8}$$

$$\frac{di_{L_t}}{dt} = \frac{1}{L_t} \left[v_{\text{exc}} - i_{L_t} R_{\text{wdg}} - v_{C_t} \right] \tag{9}$$

$$\frac{dv_{C_t}}{dt} = \frac{1}{C_t} \left[i_{L_t} - \frac{v_{C_t} - v_{C_1}}{R_1} - \frac{v_{C_t}}{R_{\text{extra}}} - i_{\text{gun}} \right] \tag{10}$$

$$\frac{dv_{C_1}}{dt} = \frac{1}{R_1 C_1} \left[v_{C_t} - v_{C_1} \right] \tag{11}$$

with zero initial conditions. Solving (8)-(11), the voltage across the gun can be directly extracted as $v_{\text{gun}} = v_{C_t}$.

The expression of the excitation voltage v_{exc} given in Fig. 3c) is expressed in the time domain as

$$v_{\text{exc}} = \begin{cases} \frac{V_{\text{gun}}}{t_{\text{r}}} t & 0 \leq t \leq t_{\text{r}} \\ V_{\text{gun}} - V_{\text{gun}} \Delta V_{\text{cap}} \% \frac{1}{t_{\text{flat}} + t_{\text{settle}}} (t - t_{\text{r}}) & t_{\text{r}} \leq t \leq t_{\text{r}} + t_{\text{flat}} + t_{\text{settle}} \\ \left(V_{\text{gun}} \Delta V_{\text{cap}} \% - V_{\text{gun}} \right) \frac{1}{t_{\text{f}}} \left[t - (t_{\text{r}} + t_{\text{flat}} + t_{\text{settle}} + t_{\text{f}}) \right] & t_{\text{r}} + t_{\text{flat}} + t_{\text{settle}} \leq t \leq t_{\text{r}} + t_{\text{flat}} + t_{\text{settle}} + t_{\text{f}} \\ 0 & \text{otherwise} \end{cases}$$

while the gun characteristic given in Fig. 3d) is modelled as

$$i_{\text{gun}} = \begin{cases} \frac{I_{\text{gun}}}{0.5 V_{\text{gun}}} v_{\text{gun}} & 0 \leq v_{\text{gun}} \leq \frac{1}{2} V_{\text{gun}} \\ I_{\text{gun}} & \frac{1}{2} V_{\text{gun}} \leq v_{\text{gun}} \leq V_{\text{gun}} \end{cases}$$

In order to reduce the computational effort of the optimization and evaluate the behaviour of the pulse during the transient period, the equations (8)-(11) are solved for only a short time interval t_{short} at the beginning of the pulse, which is given by

$$t_{\text{short}} = t_{\text{settle}} + t_{\text{add}}$$

with $t_{\text{add}} = 1\,\mu s$. The gun voltage is calculated for this time period and the transient characteristics of the pulse are checked. The considered rise time t_{rise} and the overshoot os are defined as

$$t_{\text{rise}} = t_{100} - t_{50} \qquad os = \left(\frac{V_{\text{max}}}{V_{\text{nom}}} - 1 \right) \cdot 100\%$$

To calculate the rise time (50%-100%) of the pulse, the two points in time t_{50} and t_{100} are used, which indicate the time instances where the voltage pulse reaches 50% and 100% of its nominal value. For calculating the overshoot, the maximum voltage V_{max} is determined and the os is compared to the predefined acceptable overshoot given in the specifications. The settling time ends when the voltage pulse lies completely inside the FTS_{lim} band. By stepping through $v_{\text{gun}}(t)$ in the time domain, the settling point in time is obtained. At step S8 the rise and settling times as well as overshoots are stored for evaluating the different pulse shapes and visualizing the data. In case one or more pulse characteristics do not meet the specifications, the inner loop sets a new set of values for R_1, C_1, R_{extra} and step S8 is repeated for the new set of the DN parameters values. If all values for R_1, C_1 and R_{extra} have been considered, the procedure starts again with step S1, which defines a new set of design variables. In case all transient characteristics are met, the design is considered to be valid and the "energy losses" during the settling and the fall time are computed by integrating the power over these intervals (S9). Also, the usable energy during the flat-top is determined. With these values, the pulse efficiency η_{pulse} results

$$\eta_{\text{pulse}} = \frac{E_{\text{flat-top}}}{E_{\text{settling}} + E_{\text{flat-top}} + E_{\text{fall}}}$$

where $E_{\text{flat-top}}, E_{\text{settling}}, E_{\text{fall}}$ are the energies during flat-top, until flat-top is reached and during fall time, respectively. The resulting pulse efficiency and the transformer volume are a point of the Pareto front. In a next step, the procedure restarts with S1 through the outer loop and a new valid design is calculated. Finally, in S10 the Pareto front of pulse efficiency versus transformer volume is plotted.

The same basic procedure is applied for the other DN types as well. For DN type 2 the set of equations is

$$\bar{x}_{\text{type 2}} = \left[i_{L_t}, \, i_{L_2}, \, v_{C_t} \right]^{\text{T}} \tag{12}$$

$$\frac{di_{L_t}}{dt} = \frac{1}{L_t} \left[v_{\text{exc}} - i_{L_t} R_{\text{wdg}} - v_{C_t} \right] \tag{13}$$

$$\frac{di_{L_2}}{dt} = \frac{R_2}{L_2 \left(R_2 + R_{\text{extra}} \right)} \left[v_{C_t} - R_{\text{extra}} \left(i_{L_2} - i_{\text{gun}} \right) \right] \tag{14}$$

$$\frac{dv_{C_t}}{dt} = \frac{1}{C_t} \left[i_{L_t} - \frac{1}{R_2 + R_{\text{extra}}} \left(v_{C_t} + R_2 i_{L_2} + R_{\text{extra}} i_{\text{gun}} \right) \right] \tag{15}$$

while for DN type 0 becomes

$$\bar{x}_{\text{type 0}} = \left[i_{L_t}, \, v_{C_t} \right]^{\text{T}} \tag{16}$$

$$\frac{di_{L_t}}{dt} = \frac{1}{L_t} \left[v_{\text{exc}} - i_{L_t} R_{\text{wdg}} - v_{C_t} \right] \tag{17}$$

$$\frac{dv_{C_t}}{dt} = \frac{1}{C_t} \left[i_{L_t} - i_{\text{gun}} \right] \tag{18}$$

with zero initial conditions. For the varistors in DN type 3, a simplified model is assumed, where an infinite resistance below a certain threshold voltage V_{var} is assumed and the varistors start to conduct instantaneously at the threshold voltage offering a low resistance path. As a result, below V_{var} DN type 3 acts as a DN type 0 with the additional R_{extra} and as a DN type 1 above this voltage.

After evaluating all the different DN types the optimization routine is finished. In the following section, the routine is applied for the design of the transformer and the damping network for the CARM modulator system.

4 CARM Source Modulator Case Study

At the research center ENEA, a cyclotron autoresonance maser (CARM) is currently under development which is a mm-wavelengh source. For this system, a pulsed modulator is required with the specifications listed in Table I. The optimization routine presented in section 3 is applied to the specifications to validate its performance.

4.1 Component & Parameter Selection

Before starting the optimization procedure, the components and some parameters are defined as provided in Table II. There, the 5 degrees of freedom are given, which are illustrated in Fig. 5a). Due to the required ultra-fast rise time, the primary winding is chosen to have only 1 turn. This minimizes the leakage inductance, which is a limiting factor for the rise time. The 5SNA1250B450300 IGBT is considered as pulse switch which has been successfully used in [1] with a switching capability of 12 MW (3 kV / 4 kA). The switching characteristics of the IGBT are directly taken from the datasheet. A 100 nH parasitic inductance referred to the primary side is considered for the SUs [17].

The transformer is immersed into a tank, which is filled with an insulating mineral oil with a specific relative permittivity $\varepsilon_{\text{r,oil}}$. According to [17], a peak electric field strength E_{th} of 20 kV/mm is acceptable for mineral oil and for short pulse lengths in the range of a few µs. To the turn with the highest voltage a field shape ring is attached which lowers the maximum E-field. The field shape ring is designed with a radius d_{f}, so that $E_{\text{max}} < E_{\text{th}}$. In [1, 17], the field shape ring had a 7 mm radius. Here, a more conservative value of 9 mm is selected, as optimization runs of the transformer design showed a tendency between the range of 8-9 mm for not exceeding E_{max}. Moreover, in this analysis, silicon iron (SiFe) 3% with a tape thickness of 50 µm is assumed as core material due to its high saturation flux density and high interlaminate breakdown voltage [1, 13]. A 1.5 T applied flux density is assumed for the SiFe core. The gun has a 100 pF parasitic capacitance while an additional 50 pF is considered for the HV capacitive voltage divider. The gun is placed in the same oil tank as the transformer, so that no high voltage cable is needed. In contrast to the genetic-based optimization algorithm in [5], the optimization routine runs in a brute-force mode for the 5 degrees of freedom. This allows a better understanding of how the combination of the different transformer geometries with the four DN types relate to each other.

4.2 CARM Transformer Design

Two SUs, which lead to a transformer with 1 core, are sufficient to provide the rated power of the gun. However, apart from a 1 core transformer, also 2 and 3 core transformer arrangements are examined. The lower and upper boundaries of the 5 degrees of freedom are given in Table II. For the three considered transformer core numbers,

Table IV: Considered boundaries for the parameters of the DN types.

N_c	DN type 1	DN type 2	DN type 3
1	$1\,\mathrm{k\Omega} \leq R_1 \leq 15\,\mathrm{k\Omega}$ $50\,\mathrm{pF} \leq C_1 \leq 50\,\mathrm{nF}$	$0.1\,\mathrm{k\Omega} \leq R_2 \leq 5\,\mathrm{k\Omega}$ $1\,\mathrm{\mu H} \leq L_2 \leq 5\,\mathrm{mH}$	$1\,\mathrm{k\Omega} \leq R_{3a} \leq 15\,\mathrm{k\Omega}$ $50\,\mathrm{pF} \leq C_{3a} \leq 50\,\mathrm{nF}$ $1\,\mathrm{k\Omega} \leq R_{3b} \leq 15\,\mathrm{k\Omega}$ $50\,\mathrm{pF} \leq C_{3b} \leq 50\,\mathrm{nF}$
	$R_{\mathrm{extra}} = \left\{ \frac{1}{3}R_{\mathrm{gun}}, R_{\mathrm{gun}}, \infty \right\}$	$R_{\mathrm{extra}} = \left\{ \frac{1}{3}R_{\mathrm{gun}}, R_{\mathrm{gun}}, \infty \right\}$	$R_{\mathrm{extra}} = \left\{ \frac{1}{3}R_{\mathrm{gun}}, R_{\mathrm{gun}}, \infty \right\}$
2	$1\,\mathrm{k\Omega} \leq R_1 \leq 15\,\mathrm{k\Omega}$ $50\,\mathrm{pF} \leq C_1 \leq 50\,\mathrm{nF}$	$0.1\,\mathrm{k\Omega} \leq R_2 \leq 5\,\mathrm{k\Omega}$ $1\,\mathrm{\mu H} \leq L_2 \leq 5\,\mathrm{mH}$	$1\,\mathrm{k\Omega} \leq R_{3a} \leq 15\,\mathrm{k\Omega}$ $50\,\mathrm{pF} \leq C_{3a} \leq 50\,\mathrm{nF}$ $1\,\mathrm{k\Omega} \leq R_{3b} \leq 15\,\mathrm{k\Omega}$ $50\,\mathrm{pF} \leq C_{3b} \leq 50\,\mathrm{nF}$
	$R_{\mathrm{extra}} = \left\{ \frac{1}{7}R_{\mathrm{gun}}, \frac{1}{3}R_{\mathrm{gun}}, \infty \right\}$	$R_{\mathrm{extra}} = \left\{ \frac{1}{7}R_{\mathrm{gun}}, \frac{1}{3}R_{\mathrm{gun}}, \infty \right\}$	$R_{\mathrm{extra}} = \left\{ \frac{1}{7}R_{\mathrm{gun}}, \frac{1}{3}R_{\mathrm{gun}}, \infty \right\}$
3	$1\,\mathrm{k\Omega} \leq R_1 \leq 15\,\mathrm{k\Omega}$ $50\,\mathrm{pF} \leq C_1 \leq 50\,\mathrm{nF}$	$0.1\,\mathrm{k\Omega} \leq R_2 \leq 5\,\mathrm{k\Omega}$ $1\,\mathrm{\mu H} \leq L_2 \leq 5\,\mathrm{mH}$	$1\,\mathrm{k\Omega} \leq R_{3a} \leq 15\,\mathrm{k\Omega}$ $50\,\mathrm{pF} \leq C_{3a} \leq 50\,\mathrm{nF}$ $1\,\mathrm{k\Omega} \leq R_{3b} \leq 15\,\mathrm{k\Omega}$ $50\,\mathrm{pF} \leq C_{3b} \leq 50\,\mathrm{nF}$
	$R_{\mathrm{extra}} = \left\{ \frac{87}{1000}R_{\mathrm{gun}}, \frac{1}{7}R_{\mathrm{gun}}, \infty \right\}$	$R_{\mathrm{extra}} = \left\{ \frac{87}{1000}R_{\mathrm{gun}}, \frac{1}{7}R_{\mathrm{gun}}, \infty \right\}$	$R_{\mathrm{extra}} = \left\{ \frac{87}{1000}R_{\mathrm{gun}}, \frac{1}{7}R_{\mathrm{gun}}, \infty \right\}$

an optimization run is performed up to the step S6 of the design procedure given in Fig. 5. There, all the different combinations of L_t, C_t are stored. The results are given as a scatter plot in Fig. 6. The green curves in Fig. 6 indicate the pareto fronts, which are used in order to identify the optimal ranges of the parasitics of each considered core number and they are listed in Table III. These ranges are used for the design of the DN types. It can be seen that the higher the number of cores, the lower the parasitics as predicted by the relations (1) and (2). Given that the primary winding has only a single turn, the higher number of cores results in a smaller turns ratio according to (1), which results in a smaller leakage inductance. Also, the generator inductance on the secondary side is reduced as it is inverse proportional to the number of cores.

4.3 Evaluation of Pulse Performance with the DN Types

The considered boundaries for the parameters of the DN types 1, 2 and 3 are given in Table IV. For all DN types, only R_{extra} varies when N_c increases whereas the rest of the DN parameters remain unchanged. The reason is that with an increasing N_c, the switching power capability of the system, which is $(2N_c)12\,\mathrm{MW}$, also rises as more SUs can be used. Therefore, R_{extra} is chosen to drop until the minimum point, so that the $2N_c$ SUs can just deliver the total power of the system. By reducing R_{extra}, the high output impedance of the system due to the gun decreases, which improves the pulse damping.

Using the ranges of the parasitics obtained in the previous section for each number of cores, the circuit of Fig. 3a)
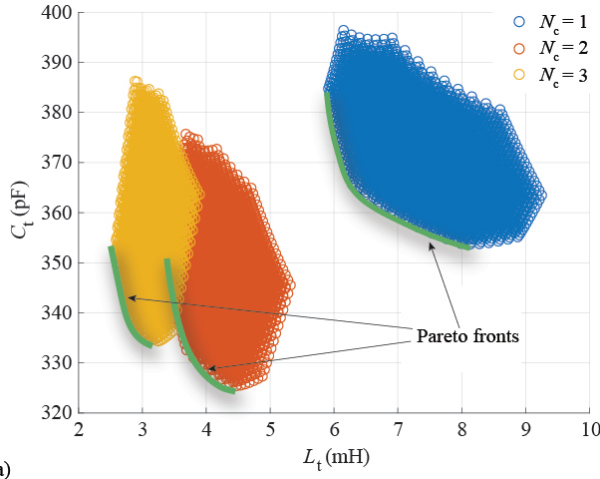

a)

Table III: Boundaries of the optimal set L_t & C_t

N_c	L_t (mH)	C_t (pF)
1	5.9 - 8.1	354 - 385
2	3.4 - 4.4	325 - 350
3	2.5 - 3.2	334 - 353

Fig. 6: a) Plots of total parasitic inductance L_t versus total parasitic capacitance C_t for a transformer with $N_c = 1, 2, 3$ cores. The green curves indicate the pareto fronts. A higher number of cores results in lower parasitics. Table III presents the respective boundaries of the parasitics extracted from the pareto curves.
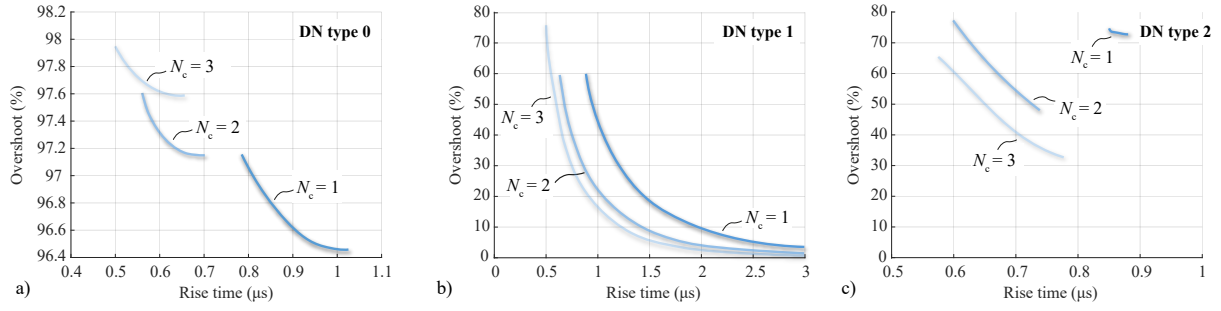
Fig. 7: Rise time versus overshoot for the considered number of cores and for DN type 0 in a), for DN type 1 in b) and for DN type 2 in c). DN type 0 results in acceptable rise times at very high overshoots. DN type 1 shows an improved performance with a good compromise between overshoot and rise time. DN type 2 results in acceptable rise times but higher overshoots than DN type 1.

is solved analytically with the four DN types. Hence, the rise time versus overshoot dependency can be extracted for all the DN types and the number of cores. This is illustrated in Fig. 7 as Pareto fronts. It is observed that DN type 0 achieves the required 1 μs rise time specification, but it results in unacceptable overshoots between 96.4% to 97.9%. It is also seen that a higher number of cores results in faster rise times due to the reduced parasitics. With DN type 1, an improved performance for the pulse could be achieved compared to the DN type 0. For instance, an overshoot of 16% can be achieved in case a transformer with 3 cores is used, at the 1 μs rise time limit. However, if a less strict rise time limit of, e.g 2μs, would be allowed for the application, the overshoot decreases rapidly to 3.5% and also the number of cores can drop to 2 as only a slight increase of 1% is observed in the overshoot between a 2 and a 3-core transformer. The performance of DN type 2 lies between DN type 0 and DN type 1. It offers comparable rise times as DN type 0 but it results in higher overshoots than DN type 1 between 32% to 78%. Also, high inductance values in the mH range would have to be realized for inductor L_2 in order to achieve lower overshoots.

In a next step, DN type 1 is extended by inserting varistors in series to the RC branch forming the DN type 3. The idea is to have the varistors in an "off-state" operation below a certain threshold value because without damping (i.e DN type 0) the rise times are below 1 μs. By "activating" the varistors above a certain threshold value, the overshoot in Fig. 7a) should be reduced. In order to examine the influence of different threshold (clamping) voltages of the varistors two values are assumed, which are $V_{var} = 350$ kV and $V_{var} = 500$ kV for 1 varistor branch. The results are presented in Fig. 8a) and b), respectively. For $V_{var} = 350$ kV, the overshoot is 32%, 13%, and 8% at the 1 μs rise time limit when the number of cores is 1, 2 and 3, respectively. On the other hand, for $V_{var} = 500$ kV clamping voltage, an overshoot of 13.6%, 4.5%, and 3.5% for 1, 2 and 3 cores is obtained at the rise time limit of 1 μs. This constitutes a relative improvement of 73%, 80%, and 80.4% compared to DN type 1 and an improvement of 57.5%, 65.4%, and 56.25% in case a 350 kV clamping voltage is used. As a last step, two parallel connected varistor branches are examined for the DN type 3 arrangement assuming $V_{var} = 500$ kV for both varistors. The rise time versus overshoot dependency for this case can be seen in Fig. 8c). It offers significantly lower overshoot levels for all the considered number of cores compared to the case with 1 varistor branch. At the 1 μs rise time limit it shows overshoots of 6%, 2%, and 1.5% for 1, 2 and 3 cores respectively. This constitutes a relative improvement of 55.9%, 55.6%, and 57.1%. Consequently, the DN type 3 with two varistor branches, a 500 kV clamping voltage and a 3 core transformer shows the best performance of all considered DN types.
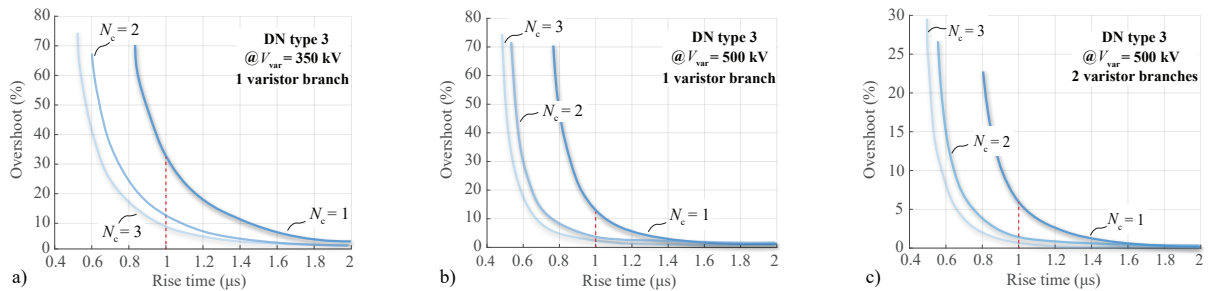

Fig. 8: Rise time versus overshoot for the considered number of cores for DN type 3 at $V_{var} = 350$ kV and 1 varistor branch in a) at $V_{var} = 500$ kV and 1 varistor branch in b) and at $V_{var} = 500$ kV and 2 varistor branches in c). A clamping voltage of 500 kV results in a better pulse performance compared to a 350 kV at the 1 μs rise time limit and for all the considered number of cores. The 2 varistor branches offer lower maximum overshoot levels and an improved performance at the 1 μs rise time limit compared to the 1 varistor branch.

Table V: Transformer, DN & pulse shape parameters for different rise times and for a 3 core transformer with DN type 3 and 2 varistor branches

Scenario	L_t(mH)	C_t(pF)	V_{var}(kV)	R_{3a}(kΩ)	C_{3a}(nF)	R_{3b}(kΩ)	C_{3b}(nF)	R_{extra}(kΩ)	t_{rise}(μs)	$t_{settling}$(μs)	os(%)	FTS(%)
1	2.6	342	500	1.5	50	1.9	50	∞	1	4.95	1.56	1.7
2	2.6	342	500	1.4	50	1.9	50	∞	1.25	4.7	0.7	1
3	2.6	342	500	1.9	35	1.9	40	12.5	1.6	4.4	0.37	0.6
4	2.6	342	500	1.9	35	2.5	30	7.61	1.76	4.6	0.31	0.4
5	2.6	342	500	1.85	27	2.45	35	7.61	2.35	3.53	0.03	0.1

Besides the rise time and the overshoot, another important transient characteristic of the pulse is the settling time. A high settling time means a long operation of the gun at a high voltage, which could result in a breakdown. Here, a 5 μs settling time limit is assumed for the voltage pulse and the achievable settling times and the pulse shapes during the transient period are investigated in a next step. For this, in Table V the transformer, DN type, and the pulse shape parameters are listed for different rise time scenarios. When the rise time is at 1 μs, the minimum achievable FTS is 1.7% having a settling time close to the limit. If one allows a longer rise time limit, the FTS limit can be reduced and the settling times become shorter. Also, the sizes of the capacitors of the 2 varistor branches tend to be lower. However, the resistor R_{extra} should be inserted to improve the pulse damping.

Among the 5 different scenarios, scenario 5 is considered to be a good compromise as it offers the best balance between the different transient characteristics. It reaches the 0.1% FTS limit at 3.53 μs with a negligible overshoot having a rise time of 2.35 μs. The pulse shape for this case is illustrated in Fig. 9a) whereas in Fig. 9b) a zoomed view is presented, where it is shown that the pulse safely lies within the FTS limit after its settling. Although the pulse shows a high rise time, it has a very fast settling time with almost zero overshoot. The fast settling time along with the insignificant overshoot are more important aspects for the pulse shape than the rise time by itself as they enable low volt-seconds during its transient interval. The volt-seconds of the pulse correlate with the breakdown voltage of the oil-immersed transformers as it has been shown in [20] and therefore should be kept low.
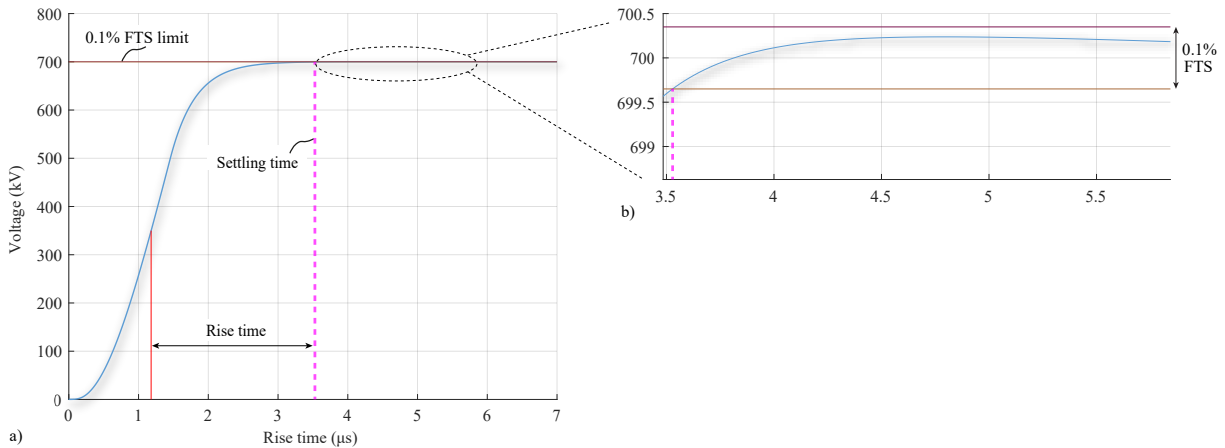

Fig. 9: a) Resulting pulse shape for the scenario 5. The pulse has a rise time of 2.35 μs and an overshoot of 0.03%. The 0.1% FTS limit can be achieved at a settling time of 3.53 μs. b) Zoomed view of the pulse after its settling. The pulse safely remains within the FTS limit.

5 Conclusion

In this paper, an extended optimization procedure is presented which combines the design of the transformer and the design of a damping network for short-pulse transformer-based solid-state modulators. In the procedure, four different DN types are considered. To validate the performance of the optimization routine, it is applied to the specifications of the CARM modulator system and a feasibility analysis is conducted for this system. Based on the given evaluation and comparison of the different damping network types, the performance of the presented design and optimization procedure is demonstrated. With this procedure, other damping network types can also be efficiently evaluated. Finally, the optimization procedure is general and it can be applied to various pulse lengths and different rise time ranges for achieving an optimal pulse performance and a compact transformer volume at the same time.

References

[1] D. Gerber and J. Biela, "Design of an ultraprecise 127-MW/3-μs solid-state modulator with split-core transformer," *IEEE Trans. on Plasma Science*, vol. 44, no. 5, pp. 829–838, May 2016.

[2] R. Cassel, "The evolution of pulsed modulators from the marx generator to the solid state marx modulator and beyond," in *IEEE Intern. Power Modulator and High Voltage Conf. (IPMHVC)*, 2012.

[3] J. Holma and M. J. Barnes, "The prototype inductive adder with droop compensation for the clic kicker systems," *IEEE Trans. on Plasma Science*, vol. 42, no. 10, pp. 2899–2908, 2014.

[4] M. Jaritz and J. Biela, "System design and measurements of a 115-kV/3.5-ms solid-state long-pulse modulator for the european spallation source," *IEEE Trans. on Plasma Science*, vol. 46, no. 10, pp. 3232–3239, Oct. 2018.

[5] S. Blume, M. Jaritz, and J. Biela, "Design and optimization procedure for high-voltage pulse power transformers," *IEEE Trans. on Plasma Science*, vol. 43, no. 10, pp. 3385–3391, Oct. 2015.

[6] S. Stathis, M. Jaritz, S. Blume, and J. Biela, "Efficiency potential of solid-state pulse modulators using SiC devices," in *22nd European Conf. on Power Electronics and Applications (EPE ECCE Europe)*, 2020.

[7] D. Bortis, J. Biela, G. Ortiz, and J. W. Kolar, "Design procedure for compact pulse transformers with rectangular pulse shape and fast rise times," in *IEEE Intern. Power Modulator and High Voltage Conf.*, 2010, pp. 298–302.

[8] J. Sabate, M. Schutten, R. Steigerwald, Qiming Li, and W. F. Wirth, "Ripple cancellation filter for magnetic resonance imaging gradient amplifiers," in *19th IEEE Applied Power Electronics Conf. and Exposition (APEC)*, 2004, pp. 792–796.

[9] J. Borburgh, M. Crescenti, A. Fowler, M. Hourican, K. Metzmacher, and L. Sermeus, "The design of the special magnets for PIMMS/TERA," *Proc. of EPAC*, 2004.

[10] G. Tsolaridis, N. Patzelt, and J. Biela, "Output filter with adaptive damping for interleaved converters with low ripple and high dynamics," in *21st European Conf. on Power Electronics and Applications (EPE ECCE Europe)*, 2019.

[11] C. Yamazaki, E. Ikawa, T. Yoshino, K. Sato, F. Saito, S. Nakamura, H. Matsumoto, and H. Kobayashi, "Beam acceleration experiment with developed 10 MW class high-precision power supply for accelerator electromagnets," in *Intern. Power Electronics Conf. (ECCE ASIA)*, 2010, pp. 1526–1529.

[12] I. Spassovsky, "From research and design work toward the realization of CARM source at ENEA," in *44th Intern. Conf. on Infrared, Millimeter, and Terahertz Waves (IRMMW-THz)*, 2019.

[13] M. Jaritz, T. Franz, R. Christen, M. Bucher, M. Schueller, J. Smajic, A. Stoeckli, and M. Bader, "A comprehensive design procedure for high voltage pulse power transformers," in *IEEE Pulsed Power Plasma Science (PPPS)*, 2019.

[14] J. Biela, D. Bortis, and J. W. Kolar, "Reset circuits with energy recovery for solid-state modulators," *IEEE Trans. on Plasma Science*, vol. 36, no. 5, pp. 2626–2631, 2008.

[15] H. Singer, H. Steinbigler, and P. Weiss, "A charge simulation method for the calculation of high voltage fields," *IEEE Trans. on Power Apparatus and Systems*, vol. PAS-93, no. 5, pp. 1660–1668, 1974.

[16] J. Biela, "Optimierung des electromagnetisch integrierten serien-parallel resonanzkonverters mit eingeprägtem ausgangsstrom," Ph.D. dissertation, ETH Zürich, 2005.

[17] M. S. Blume, "Highly efficient pulse modulator system with active droop compensation for linear colliders," Ph.D. dissertation, ETH Zürich, 2016.

[18] M. Jaritz, "Solid-state modulator for generating high voltage pulses in the ms-range with high output power," Ph.D. dissertation, ETH Zürich, 2018.

[19] R. Erickson, "Optimal single resistors damping of input filters," in *14th Annual Applied Power Electronics Conf. and Expos. (APEC)*, 1999, pp. 1073–1079.

[20] S. Okabe, "Evaluation of breakdown characteristics of oil-immersed transformers under non-standard lightning impulse - insulation characteristics for non-standard lightning impulse waveforms with oscillations," *IEEE Trans. on Dielectrics and Electrical Insulation*, vol. 14, no. 3, pp. 679–688, 2007.